

Iterative Self-Organizing Atherosclerotic Tissue Labeling in Intravascular Ultrasound Images and Comparison With Virtual Histology

Amin Katouzian*, Athanasios Karamalis, Debdoot Sheet, Elisa Konofagou, Babak Baseri, Stephane G. Carlier, Abouzar Eslami, Andreas König, Nassir Navab, and Andrew F. Laine, *Fellow, IEEE*

Abstract—Intravascular ultrasound (IVUS) is the predominant imaging modality in the field of interventional cardiology that provides real-time cross-sectional images of coronary arteries and the extent of atherosclerosis. Due to heterogeneity of lesions and stringent spatial/spectral behavior of tissues, atherosclerotic plaque characterization has always been a challenge and still is an open problem. In this paper, we present a systematic framework from *in vitro* data collection, histology preparation, IVUS-histology registration along with matching procedure, and finally a robust texture-derived unsupervised atherosclerotic plaque labeling. We have performed our algorithm on *in vitro* and *in vivo* images acquired with single-element 40 MHz and 64-elements phased array 20 MHz transducers, respectively. In former case, we have quantified results by local contrasting of constructed tissue colormaps with corresponding histology images employing an independent expert and in the latter case, virtual histology images have been utilized for comparison. We tackle one of the main challenges in the field that is the reliability of tissues behind arc of calcified plaques and validate the results through a novel random walks framework by incorporating underlying physics of ultrasound imaging. We conclude that proposed framework is a formidable approach for retrieving imperative information regarding tissues and building a reliable training dataset for supervised classification and its extension for *in vivo* applications.

Index Terms—Atherosclerosis, histology, intravascular ultrasound (IVUS), plaque characterization, random walks, wavelet packets.

I. INTRODUCTION

CORONARY heart disease is the most common type of heart disease and takes about 500 000 lives in the United States every year [1]. For chronic disease such as atherosclerosis that may reoccur after balloon angioplasty, atherectomy, stenting, or bypass surgery, the accurate diagnosis of vulnerable plaques (VPs) [2], [3] is critical. In brief, *what makes atherosclerosis one of the deadliest disease is not the stenosis alone but failure in detection and proper treatment of the vulnerable plaques that will lead to myocardial infarction.* Unlike other comparable imaging modalities such as optical coherence tomography and near infrared imaging that lack adequate depth of penetration, intravascular ultrasound (IVUS) provides morphological as well as pathological cross-sectional grayscale images of the arterial lumen and occluded lesions throughout arteries with sufficient penetration and resolution. The numbers of developed IVUS-based frameworks and conducted studies signify the capability of this imaging modality and the importance in an improved understanding of atherosclerosis disease. It is reasonable to conclude that the ultimate goal of any tissue characterization is the algorithmic detection of all tissue compositions, especially VPs, which are ultimately identified by an expert assessing classified tissue colormaps.

In [4], IVUS elastography (IVE) was used to cross correlate between RF signals in consecutive frames to assess local mechanical properties of plaques *in vitro* and classify tissues based on their mean strain values into fibrous, fibro-fatty, and fatty types. Additional IVE validation was reported in [5], who employed the Lagrangian speckle model estimator along with a scaling factor estimator to compute radial strain elastograms. Kawasaki *et al.* [6] incorporated integrated backscatter (IB) into IVUS (IVUS-IB) to classify tissues and delineate lipid, fibrous, and calcified tissues *in vivo*. Contrary to IVE and IVUS-IB that could not detect the necrotic core directly, Nair *et al.* presented a spectrum-based technique in combination with a classification tree to classify tissues into fibrous, fibro-fatty, necrotic, and calcified [7]. They extracted eight spectral features (intercept, slope, mid-band-fit, IB, minimum and maximum powers, and their corresponding frequencies) from a linear regression fit to calibrated tissue spectra using 30 MHz, single element rotating transducers. The first two spectral signatures (intercept,

Manuscript received February 24, 2012; revised June 12, 2012 and August 8, 2012; accepted August 10, 2012. Date of publication August 15, 2012; date of current version October 16, 2012. Asterisk indicates corresponding author.

*A. Katouzian is with the Technical University of Munich, Munich 80333, Germany, and also with the Department of Biomedical Engineering, Columbia University, New York, NY 10027 USA (e-mail: amin.katouzian@cs.tum.edu).

A. Karamalis and N. Navab are with the Technical University of Munich, Munich 80333, Germany (e-mail: karamali@in.tum.de; navab@cs.tum.edu).

D. Sheet is with Technical University of Munich, Munich 80333, Germany, on leave from School of Medical Science and Technology, Indian Institute of Technology, Kharagpur 721302, India (e-mail: debdoot.sheet@tum.de).

E. Konofagou is with the Department of Biomedical Engineering, Columbia University, New York, NY 10027 USA (e-mail: ek2191@columbia.edu).

B. Baseri is with the Medical Center of Hackensack University, New Jersey, NJ 07601 USA (e-mail: ba.baseri@gmail.com).

S. G. Carlier is with the Department of Cardiology, Universitair Ziekenhuis Brussel, Brussels B-1090, Belgium (e-mail: sgcarter@hotmail.com).

A. Eslami is with the Technical University of Munich, Munich 80333, Germany. He is also with Institute for Biomathematik and Biometrie, Helmholtz Zentrum, München 80333, Germany (e-mail: eslami@cs.tum.edu).

A. König is with the Department of Cardiology, Klinikum Innenstadt der Universität München, München 80333, Germany (e-mail: andreas.Koenig@med.uni-muenchen.de).

A. F. Laine is with the Department of Biomedical Engineering and Radiology, Columbia University, New York, NY 10027 USA (e-mail: laine@columbia.edu).

Color versions of one or more of the figures in this paper are available online at <http://ieeexplore.ieee.org>.

Digital Object Identifier 10.1109/TBME.2012.2213338

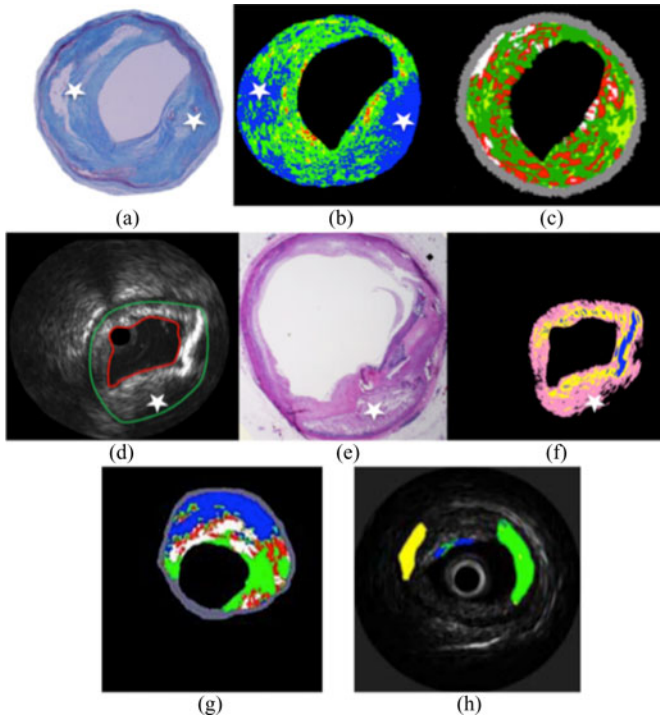


Fig. 1. Resulting distinct tissue colormaps with different available tissue characterization algorithms. (a) Histology image and (b) corresponding generated tissue colormaps via IVUS-IB and (c) IVUS-VH algorithms [19]. The red, green, and blue colors represent fibrotic, lipidic, and calcified tissues, respectively, in (b). The white, red, dark green, and light green represent calcified, necrotic, fibrotic, and fibrofatty tissues, respectively, in (c). (d) Grayscale image, (e) corresponding histology, and constructed tissue colormap through the IVUS-PH algorithm [18]. (f) Blue, yellow, and magenta colors represent calcified, fibrotic, and lipidic tissues, respectively. (g) Two distinct constructed tissue colormaps via IBH [15] and (h) error-correcting output codes (ECOC) algorithm [16]. The white, red, green, and blue colors represent calcified, necrotic, fibrotic, and shadowing areas, respectively in (g). The blue, yellow, and green colors represent calcified, lipidic, and fibrotic tissues, respectively, in (h). The white stars mark lipid pool areas.

slope), which initially were introduced by Lizzi *et al.* [8], were indicative of scatterer concentration and size. Currently, this methodology, known as IVUS-virtual histology (IVUS-VH), has been implemented in the volcano (Rancho Cordova, CA) IVUS clinical scanners using 20-MHz 64-elements phased array transducer. Previously, we investigated the reliability of extracted features, sufficiency of training dataset, and complexity of classification algorithms using single-element 40-MHz Atlantis transducers [9]. We observed large variations among spectrum-derived features using the VH technique that made characterization very challenging.

IVUS findings have shown that sonographic differences yielding visual discrimination among plaque constituents [10], [11]. In other words, variations of intensities are attributed to repetitive tissue microstructure patterns that used as a basis for texture-derived algorithms [12]–[15] as an alternative approach to their spectrum-based counterparts. This can be advantageous since usually RF signals are not accessible. However, the appearance of images may vary depending on selected parameters during acquisition [i.e., time gain compensation (TGC)], normalization, or reconstruction (i.e., nonlinear transformation) that makes the

TABLE I
EXISTING ATHEROSCLEROTIC TISSUE CHARACTERIZATION ALGORITHMS

Author (Year)	RF-Based Techniques			Texture-Based Techniques		
	IVUS-VH	IVUS-IB	IVE	ECOC	IBH	IVUS-PH
Nair <i>et al.</i> (2001) [7]		Kawasaki <i>et al.</i> (2002) [6]	de Corte <i>et al.</i> (2000) [4]	Escalera <i>et al.</i> (2009) [14,16*]	Taki <i>et al.</i> (2009) [15]	Katouzian <i>et al.</i> (2008) [18]
Fibrotic Cap	Yes (inferred)	Yes (inferred)	No	Possible***	Yes (inferred)	Yes (inferred)
Lipid Core Size	Yes	Yes	Possible****	Possible***	Possible****	Yes
Percentage of Stenosis	Yes	Yes	Yes	Possible***	Yes	Yes
Calcification	Yes	Yes	Possible****	Yes	Yes	Yes
Detection of VP	Yes (inferred)	Yes (inferred)	No	Possible***	Possible****	Yes (inferred)
Histology Validation	Yes	Yes	Yes	Yes	Yes	Yes
Tissue Types	Fibrotic Fibrofatty Calcified Necrotic	Fibrotic Lipidic Calcified	Fibrous Fibrofatty Fatty	Fibrotic Lipidic** Calcified	Fibrotic Calcified Necrotic	Fibrotic Lipidic Calcified No Tissue

* It is extension of [14] combined with spectral features.

** Replaced by "soft tissue" in [14].

*** Due to partial classification of tissues within stenosis region.

**** Could not be inferred from original publication.

tissue characterization even more challenging. Recently, a supervised classification approach with combined textural-spectral features was also proposed to characterize tissues [16]. A state-of-the-art review on existing atherosclerotic tissue characterization algorithms has been reported in [17]. Fig. 1 illustrates distinct tissue colormaps constructed with proposed algorithms in [6], [7], [15], [16], and [18]. Table I summarizes these techniques and their ability to detect factors associated with VPs.

As we can see, there is no consensus on unified tissue labels and definition of tissue types. One may classify tissues into fibrotic, lipidic, and calcified [6], [16], [18] and another translates lipidic into fibrofatty [4], [7] or fibro-lipidic. Authors in [14], [15] and [18] detect shadows behind arc of calcified plaques and add "no tissue" label, respectively, in order to take into account the uncertainty [20], [21] of classification results in these regions.

All described methods have their own advantages; however, in their clinical applications, they have been only partially successful. For example, the proposed algorithm in [16] combines both textural and spectral features, which hypothetically is a more reliable approach to tackle tissue characterization problem. On the other hand, it does not reflect the heterogeneity of tissues that is inherited in atherosclerotic plaques, classifies tissues partially within plaque, and therefore does not guide experts toward VP features such as lipid core size. In brief, there are two major concerns regarding aforementioned tissue characterization algorithms regardless of their implemented techniques: 1) the construction of reliable training dataset [9], 2) the extension of *in vitro* derived classifier for *in vivo* application without proper validation [9], [17], [40]. In this paper, we propose a systematic methodological framework from data collection, histology preparation, registration, feature extraction, and classification to achieve a reliable *in vitro* developed tissue characterization algorithm for *in vivo* applications. We further present an effective texture-derived atherosclerotic tissue-labeling algorithm using a discrete wavelet packet frame (DWPF) and a 2-D envelope detection technique introduced by Laine and Fan [22] that relies on the Hilbert transform of multiscale representations. The extracted textural features of such expansions are

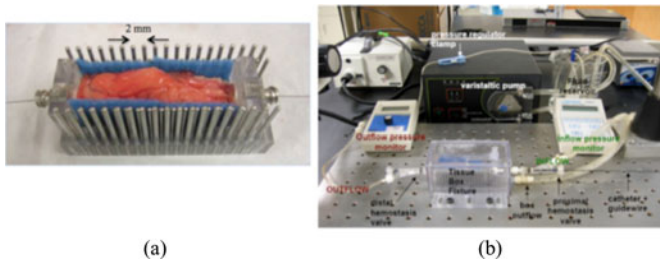


Fig. 2. (a) Tissue cage fixture *in vitro* experiment setup.

perfectly suited for classification and capturing characteristics of the plaque constitutes with the highest correlation to histology. The main advantages of our proposed technique are its independency of transducer frequency, and the construction of prognosis histology (PH) images in an unsupervised fashion that requires no manual labeling. The latter becomes crucial due to inhomogeneity of atherosclerotic tissues that makes manual labeling so challenging prior to training of supervised classification approaches. In fact, the generated PH images can be more confidently used as labeled images for training. For further validation, we apply our algorithm on images acquired with 64-elements 20-MHz phased array transducer and compare results with corresponding VH images. A primary work of the proposed technique can also be found in [18].

II. DATA COLLECTION

A. *Ex Vivo* Data Collection and Specimen Preparation

Autopsy human hearts ($n = 30$) and explanted hearts from transplant surgery ($n = 2$) were procured within 24-h post-mortem and transplantation, respectively. The major arteries were dissected from heart and attached to a circulating fluid flow system. Average length of arterial segments attached to a fluid system was 50 mm. The arterial segments [right coronary artery (RCA), left anterior descending (LAD), left circumflex (LCX)] ($n = 51$) were perfused with saline at body temperature (37°C) with pulsatile flow (60 b/min, 135 mL/min) at physiologic pressure (80–120 mmHg). A Boston Scientific (Fremont, CA) Atlantis IVUS catheter carrying single-element mechanically rotating 40-MHz transducer was then advanced along with a 0.014-in guide wire and a complete automatic pullback was performed from distal to proximal side of the specimen. The same procedure was repeated using human blood for a subset of the arterial segments ($n = 7$). Prior to the experiment, the blood was agitated by hand for approximately 1 min to mix and then stirred at low speed with a magnetic stir bar using a stir plate until the experiments began. Fig. 2 illustrates the experiment setup along with tissue box fixture. The RF data were collected using two 12-bit Acqiris boards [Monroe, NY] and digitized at periodic time intervals, $T_s = 2.5$ ns ($f_s = 400$ MHz). The catheter pullback speed and frame rate were set to 0.5 mm/s and 30 frames/s, respectively.

After imaging, the arteries were pressure fixed with 10% buffered formaldehyde followed by decalcification. The histology blocks were prepared every 2 mm (corresponding to 120

frames of the IVUS pullback) using sidebars, Fig. 2(a). All blocks were embedded in paraffin and sectioned for histological staining. Two $5\text{-}\mu\text{m}$ thick histologic cross sections were stained with hematoxylin and eosin (H&E) and Russell–Movat pentachrome. The main advantage of this methodology was that the orientation of the artery was not changed throughout the entire procedure. Therefore, more reliable IVUS-histology pairs could be obtained and the number of cross sections of interest (CSIs) per vessel was significantly increased (average of 25 regions) comparing with the traditional methods (3–5 regions) [7], [16], [23]. Although the sidebars were 2 mm apart that corresponded to 120 frames and could be used directly as indicators for systematic matching procedure we also looked for natural markers such as calcified tissues or side branches due to shrinkage of the artery and changes in plaques geometry after formalin fixation. This made the matching procedure more reliable and we selected total of 83 CSIs with more than 40% stenosis from ($n = 51$) segments.

For comparison study with VH results, we collected IVUS grayscale images from four patients using a 64-elements 20 MHz Eagle Eye transducer and s5 imaging system manufactured by VOLCANO (Rancho Cordova, CA). Typically, during percutaneous coronary intervention, a catheter was advanced from the femoral artery toward site of coronary arterial occlusion (i.e., RCA, LAD, and LCX) via aorta. During image acquisition, the catheter was pulled back from the distal to proximal locations with a speed of 0.5 mm/s, acquiring 30 frames/s.

III. METHODS

Due to heterogeneity of atherosclerotic tissues that is visible in both IVUS and histology images, see Fig. 5, a robust texture discriminator with accurate boundary detection is desirable. The latter becomes significantly important since ultrasound physics implicitly governs the change in ultrasound speed as well as textural appearance of speckles at the interface (boundary) of tissues. Hence, we chose spatial-frequency-localized orthogonal expansions such as DWPF and their generalization to 2-D in an overcomplete fashion.

The multiresolution texture analysis benefits from three main advantages: 1) there are less restrictions on filter selection, 2) the variations of the modulus in the transform domain are not corrupted by aliasing, and 3) representations are invariant to intensity profiles. Although wavelet packet decomposition is a well-established framework its implementation has high impacts on the final results and in our case the boundary accuracy. In general, they carry four main advantages over Gabor filters; 1) they cover exactly the frequency domain and provide a mathematically complete representation, 2) provides features with least correlations that is beneficial for classification, 3) they are orthogonal and therefore adaptive pruning of decomposition tree will be possible, resulting in 4) computationally fast algorithms. We describe the redundant DWPF decomposition framework that is slightly different from traditional discrete wavelet packet transform (DWPT) [24]. Unlike DWPT that was initially introduced for data compression and transmission of large content textural images, we do not decimate

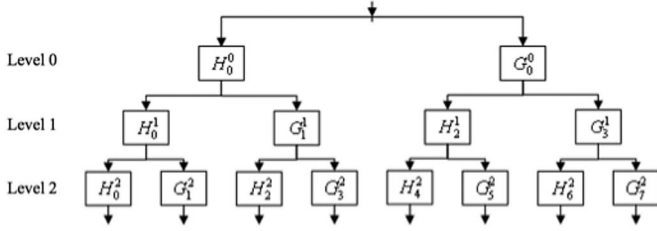


Fig. 3. Tree structure for a DWPF expansion and its associated multiscale indexes.

(downsample) data at expansion levels and try to preserve as much textural information as possible (see Fig. 3). Consequently, the redundant approach guarantees pointwise/pixelwise one-to-one bijection across levels of analysis and allows perfect representation as well as the classification of textural features. The wavelet packets are orthonormal in the space of summable-integrable functions $L^2(R)$ and described by the collection of functions $\{\xi_j(x)|j \in \mathbb{Z}^+, \langle \xi_p, \xi_q \rangle = 0, p \neq q\}$ obtained from

$$2^{l/2} \xi_{2k}(2^l x - n) = \sum_{m \in \mathbb{Z}} h_{m-2n}^l 2^{\frac{l+1}{2}} \xi_k(2^{l+1} x - m) \quad (1)$$

$$2^{l/2} \xi_{2k+1}(2^l x - n) = \sum_{m \in \mathbb{Z}} g_{m-2n}^l 2^{\frac{l+1}{2}} \xi_k(2^{l+1} x - m) \quad (2)$$

where $l, n, k, \xi_0(x) = \phi(x)$ and $\xi_1(x) = \psi(x)$ are the scale index, translation index, channel index, scaling function, and basic wavelet, respectively. Due to stringent characteristic of tissues, the proper selection of filters, g_n and h_n , becomes crucial and has significant impact on classification performance [22]. The wavelet packets at different scales can also be found by an inverse relationship as follows:

$$2^{\frac{l+1}{2}} \xi_k(2^{l+1} x - m) = \sum_n h_{m-2n}^l 2^{\frac{l}{2}} \xi_{2k}(2^l x - n) + \sum_n g_{m-2n}^l 2^{\frac{l}{2}} \xi_{2k+1}(2^l x - n). \quad (3)$$

Any function $f(x) \in L^2(R)$ can be decomposed onto a wavelet packet basis by computing the inner product $\langle f(x), \xi_k(2^l x - n) \rangle$. Using (3), we can write

$$\begin{aligned} & 2^{\frac{l+1}{2}} \int_{-\infty}^{\infty} f(x) \xi_k(2^{l+1} x - m) dx \\ &= \int_{-\infty}^{\infty} f(x) \left(\sum_n h_{m-2n}^l 2^{\frac{l}{2}} \xi_{2k}(2^l x - n) + \sum_n g_{m-2n}^l 2^{\frac{l}{2}} \xi_{2k+1}(2^l x - n) \right) dx \\ &= \sum_n h_{m-2n}^l 2^{\frac{l}{2}} \int_{-\infty}^{\infty} f(x) \xi_{2k}(2^l x - n) dx \\ &+ \sum_n g_{m-2n}^l 2^{\frac{l}{2}} \int_{-\infty}^{\infty} f(x) \xi_{2k+1}(2^l x - n) dx \quad (4) \end{aligned}$$

defining decomposition coefficients as follows:

$$\rho_{k,n}^l = 2^{\frac{l}{2}} \int_{-\infty}^{\infty} f(x) \xi_k(2^l x - n) dx. \quad (5)$$

Equation (4) can be written as follows:

$$\rho_{k,m}^{l+1} = \sum_n h_{m-2n}^l \rho_{2k,n}^l + \sum_n g_{m-2n}^l \rho_{2k+1,n}^l. \quad (6)$$

Using (1) and (2), the coefficients are calculated by

$$\rho_{2k,n}^l = \sum_m h_{m-2n}^l \rho_{k,m}^{l+1} \quad (7)$$

$$\rho_{2k+1,n}^l = \sum_m g_{m-2n}^l \rho_{k,m}^{l+1}. \quad (8)$$

As we can see, the decompositions are performed on both low and high frequency components. Therefore, a tree-structure multiband extension of the standard wavelet transform is constructed. Taking the Fourier transform of both sides of equations (7) and (8) yields

$$\Upsilon_{2k}^l(\omega) = H^l(\omega) \Upsilon_k^l(\omega) \quad (9)$$

$$\Upsilon_{2k+1}^l(\omega) = G^l(\omega) \Upsilon_k^l(\omega) \quad (10)$$

where $\Upsilon_k^l(\omega)$ is the Fourier transform of the frame coefficients at channel k and level l . This can be seen as subband filtering in frequency domain, which ultimately behaves like a filter bank with channel filters $\{F_k^l(\omega)|0 \leq k \leq 2^l - 1\}$ where $F_k^l(\omega)$ can be derived recursively as follows:

$$F_0^0(\omega) = G^0(\omega), F_1^0(\omega) = H^0(\omega) \quad (11)$$

$$F_{2k}^{l+1}(\omega) = H^{l+1}(\omega) F_k^l(\omega) = H^0(2^{l+1}\omega) F_k^l(\omega) \quad (12)$$

$$F_{2k+1}^{l+1}(\omega) = G^{l+1}(\omega) F_k^l(\omega) = G^0(2^{l+1}\omega) F_k^l(\omega). \quad (13)$$

A. Filter Selection, Feature Extraction, and Classification

The filter candidates must satisfy necessary criteria such as symmetry as well as boundary accuracy and have optimal frequency response. Hence, we selected Lemarie-Battle [25] filters that are symmetric (have linear phase response with no complicated distortion) and satisfy quadrature mirror filter criteria that covers the whole frequency spectrum and avoid having multilobe subbands in filter bank. The former property alleviates boundary effects through simple methods of mirror extension. Fig. 4 illustrates the Lemarie-Battle wavelet of order 17 and constructed filter bank at level 4. We truncated the filters to finite length and deployed separable tensor products, $F_{i \times l}^l(\omega_r, \omega_\theta) = F_i^l(\omega_r) F_j^l(\omega_\theta)$, to extend it to 2-D and extract features with particular orientation across the decomposition tree. r and θ are the axial and lateral indexes, respectively. Once the features were extracted at each level and channel, we constructed the feature matrix, $V_{i,j}^{l,k}$ as follows:

$$V_{i,j}^{l,k} = \{e_{i,j}^{l,k} | 0 \leq k \leq (2^l - 1), i, j = 1, \dots, M\} \quad (14)$$

where $e_{i,j}^{l,k}$ represents the envelope value of pixel (i, j) for the k th channel at level l .

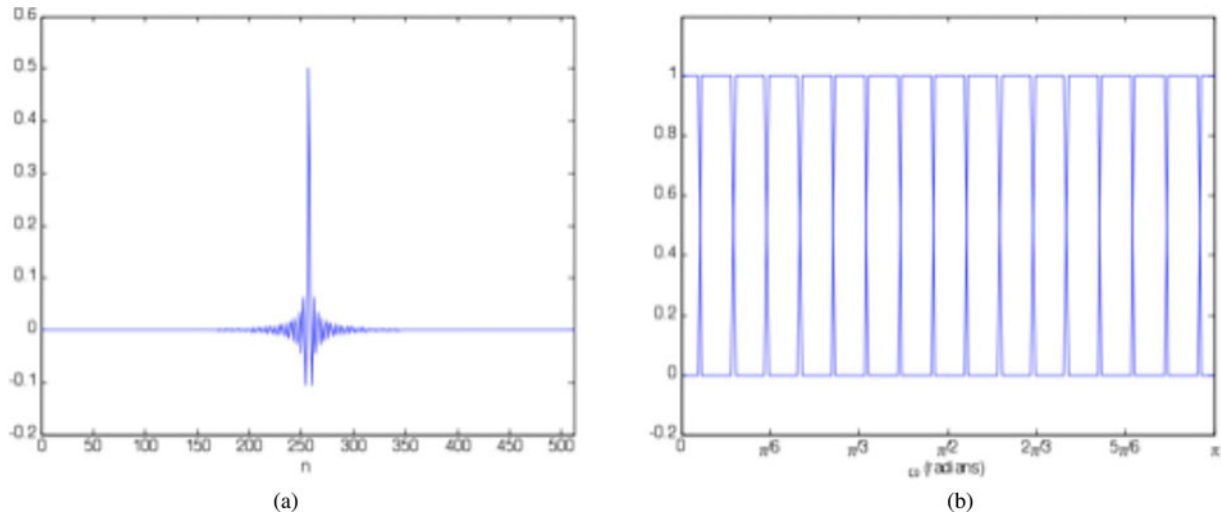


Fig. 4. (a) Lemarie–Battle filter of order 17. (b) Constructed filter bank at level 4.

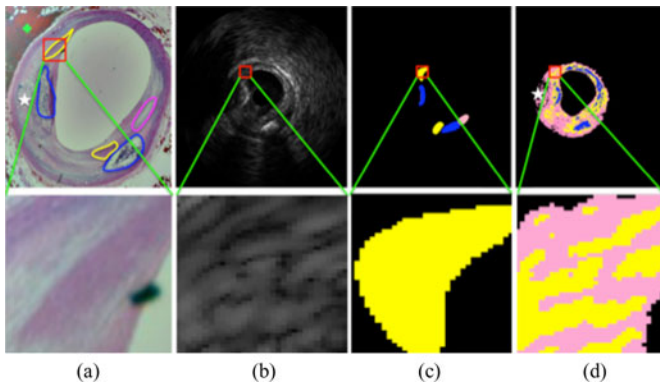


Fig. 5. (a) H&E histology image of CSI with manually segmented ROIs, (b) corresponding IVUS grayscale image, (c) manually selected regions corresponding to presumably homogenous regions for each tissue type, and (d) corresponding PH image. The bottom row illustrates the magnified version of selected ROI (red square) for fibrotic tissue. The heterogeneity of atherosclerotic tissues are well reflected in (a), (b), and (d). The white star points to lipid rich pool region that could be a sign of VP if a thin fibrotic layer existed on top of it.

As we mentioned before, because of stringent characteristics of atherosclerotic tissues and backscattered IVUS signals, a segmentation algorithm with robust boundary accuracy is demanded in order to reliably represent distinct tissue textures due to change in tissue/medium (e.g., late necrotic that lacks of cellular matrix) or tissue/tissue interfaces. As depicted in Fig. 5, the heterogeneity of tissues is clearly seen in the magnified region of histology image and corresponding region in the IVUS grayscale counterpart. Consequently, the implementation of envelope detection technique becomes crucial. We deployed a zero crossing technique [22] that is less sensitive to noise and more robust to boundaries. In this method, the maximum absolute value of extracted features was found and then assigned to adjacent zero crossing intervals. Fig. 6 demonstrates the performance of the proposed technique in comparison with the Hilbert transform method. The separable property in tensor product extension allowed us to extend the envelope detection technique

to 2-D by applying the 1-D algorithm on extracted horizontal, vertical, and diagonal features, column-wise, row-wise, and column-wise across the scales and channels, respectively.

Although existing algorithms take advantage of supervised classifier, we design our framework upon unsupervised characterization of tissues for two reasons. First, in a classical classification problem, it is widely well known [26] that an unsupervised algorithm shall be deployed if we are not able to build training or testing datasets, which in our application, the later is the case due to the heterogeneity of atherosclerotic tissues. Second, we hypothesized that deploying an unsupervised classifier, if extracted signatures represent true characteristics of atherosclerotic tissues, may result in more consistent training dataset. In other words, the result of unsupervised classifier can be utilized as a reliable alternative method for manual labeling. For this reason, we chose the iterative self-organizing data analysis (ISODATA) clustering algorithm [26] in order to generate PH images. The main advantage of ISODATA over the previous method [18] using the k -mean classifier is that the number of classes (tissues) is not required to be fixed and the algorithm automatically merges and splits the clusters. As a tradeoff, the computational speed is increased.

For every feature representation matrix, $V_{M \times M}$, a label was assigned to each pixel by modulo N_c (number of classes). We computed the center of clusters $\{C_k | 0 \leq \kappa \leq N_c - 1\}$ by calculating the mean vector for each class. The pixel $\{v_{i,j} | i, j = 1, \dots, M\}$ was assigned to the class κ , if the Euclidean distance between the corresponding pixel and the class center C_k was the closest. The centers of clusters were updated through an iterative fashion by recomputing the relative mean vectors. The clusters were possibly merged if the empirically selected threshold value for distance between two clusters were met. The number of clusters per plaque (PH image) could vary between 3 and 4, depending on presence of calcified tissues since fibrotic and lipidic tissues were repeatedly found in atherosclerotic plaques in addition to background (no tissue). The procedure was terminated once no change in labeling occurred.

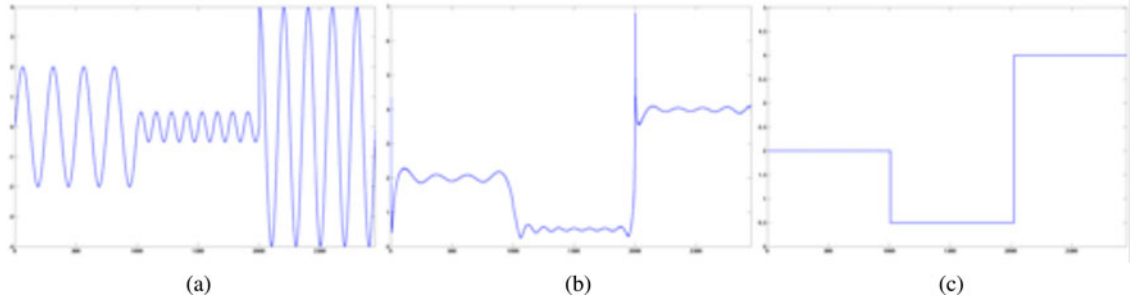


Fig. 6. (a) Arbitrary signal, (b) resulting envelope detected signal through the Hilbert transform, and our zero crossing technique.

B. Ultrasonic Signal Confidence Estimation

The acoustic shadowing in the grayscale IVUS images, caused by the attenuation of signals in dense calcified or fibrotic tissues, limited lesion assessment in these regions [31], [32]. Recent developed algorithms have also taken this limitation into account by detecting these shadow regions automatically either by the use of local grayscale statistics [14] or global thresholding [33]. It is worth mentioning that even though shadow region is short of informative tissue features its interpretation remains very important since it can be a sign of late necrotic core where extracellular matrix totally lacks of collagen. In order to examine the possibility of presence of adequate signal information, we deployed a confidence estimation technique that modeled this problem as a random walk framework motivated by the physic property of ultrasound [34], [35].

Preliminary to presenting our own approach, we provide a brief overview of the original random walk technique where the user places seeds/labels in regions for multilabel segmentation. The target image or volume is handled as a discrete object by representing pixels as nodes $v \in V$ that are connected by weighted $w_{i,j}$ edges $e_{i,j} \in E$; forming a graph Laplacian $G = (V, E)$. Subsequently, the probability of a random walk reaching first one of the label nodes is computed for every unlabeled node in the graph. The analytic solution to the desired probabilities is derived from the Laplacian matrix:

$$L_{i,j} = \begin{cases} d_i & i = j \\ -w_{i,j} & v_i \text{ and } v_j \text{ are adjacent nodes} \\ 0 & o.w. \end{cases} \quad (15)$$

where $d_{i,j} = \sum_j w_{i,j}$ and $w_{i,j}$ are the weight connecting two nodes v_i and v_j . In the original work, a Gaussian weighting function was chosen $w_{i,j} = \exp(-\beta(g_i - g_j)^2)$, where g_i is the pixel intensity at i th node and β is the only free parameter of the method, which is set to a constant value for all experiments in the original and our own work ($\beta = 90$). To obtain the solution and to practically apply the necessary boundary conditions imposed by the labeled nodes, L is reordered and decomposed into blocks of marked M and unmarked nodes U :

$$L = \begin{bmatrix} L_M & B \\ B^T & L_U \end{bmatrix}. \quad (16)$$

The desired probabilities are obtained by solving $L_U x_U = -B^T x_M$, where x_U and x_M are the unknown and known probabilities for the unmarked and seed nodes, respectively.

For confidence estimation manual seed placement is replaced by automatic one. The virtual transducer element nodes are placed at the beginning and “no signal “ nodes at the end of each scanline, as illustrated in Fig. 9(a). We can estimate the confidence maps on either RF data or grayscale images in polar coordinates. Therefore, an equidistant lattice representation is used along with modified weighting function to adjust the random walk framework to our problem by incorporating ultrasound transmission properties. The new function is given as follows:

$$w_{i,j} = \begin{cases} w_{i,j}^H & \text{if } i \text{ and } j \text{ are adjacent and } e_{i,j} \in E^H \\ w_{i,j}^D & \text{if } i \text{ and } j \text{ are adjacent and } e_{i,j} \in E^D \\ w_{i,j}^V & \text{if } i \text{ and } j \text{ are adjacent and } e_{i,j} \in E^V \\ 0 & o.w. \end{cases} \quad (17)$$

$$w_{i,j}^H = \exp(-\beta(c_i - c_j)^2 + \gamma) \quad (18)$$

$$w_{i,j}^D = \exp(-\beta(c_i - c_j)^2 + \sqrt{2}\gamma) \quad (19)$$

$$w_{i,j}^V = \exp(-\beta(c_i - c_j)^2) \quad (20)$$

where E^H , E^D , and E^V are the edges along horizontal, diagonal, and vertical graph directions, respectively, see Fig. 9(a), $c_i = r_i \exp(-\alpha x_i)$, α is the attenuation coefficient (set to $\alpha = 2$), and r_i is the absolute value of RF signal or pixel intensity. The x_i is normalized closest distance from node v_i to the virtual transducer elements (seeds). The decrease in acoustic energy (ultrasound transmission) implies the decrease of confidence in the data. More specifically, the ultrasound is reflected and transmitted at the boundary of tissues with different acoustic impedances. Reflected and transmitted energy are negatively related, i.e., the stronger the reflection the lower the transmission and vice versa [36]. Consequently, strong echoes in the acquired RF signal or images indicate decrease in transmission and thus decrease in confidence. In the random walks formulation, the gradient $c_i - c_j$ expresses this phenomenon as the overall probability for a node decreases with decreasing weights (increasing resistance) along the random walk path. Contrary to original random walk framework, the randomness shall be resolved since transmitted signal is focused at certain point within transducer beam-width along each scanline. This is realized by additive parameter γ that penalizes diagonal and horizontal walks away from each scanline where the walk is initiated from. As we can see, the probability of diagonal and horizontal walks decreases

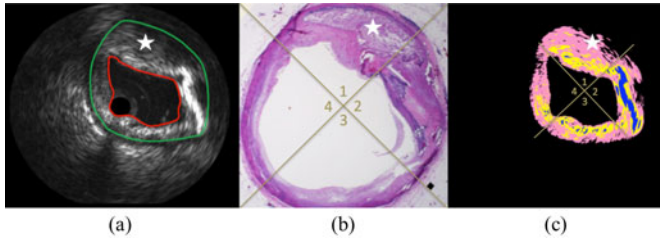


Fig. 7. (a) Manually traced vessel wall (green) and lumen border (red) on IVUS B-mode image, (b) corresponding H&E histology image, (c) constructed PH image (blue, yellow, and magenta colors represent calcified, fibrotic and lipidic components). The white star points to lipid rich pool region that could be sign of VP if thin fibrotic layer existed on top of it. For classified tissues, the histopathologist reported composite scores in four quadrants.

when walking away from transducer along scanline. Moreover, we adopted the Beer–Lambert law in function c_i to take into account the attenuation of signals in our model.

IV. EXPERIMENTAL RESULTS AND QUANTIFICATION ANALYSIS WITH DISCUSSION

We processed the IVUS signals from each raw data frame, represented in the (r, θ) domain, which is the original domain of acquisition, containing 256 lines that span over 360° with 2048 samples per line. In order to have an optimal frame size with respect to its computational complexity and textural resolution, we decimated and interpolated (via a spline) the signals in axial and lateral directions, respectively, to generate square $M = 512$ pixels frame. Both decomposition and ISODATA algorithms were implemented in C++. All computations were executed on an IBM ThinkStation workstation, 64-bit 3 GHz dual Intel Core2Quad Processors with 32 GBs of RAM. The execution time for each CSI was evaluated to be 22 ms.

Eighty-three CSIs collected from 51 segments of 32 hearts *ex vivo*, including 19 LADs, 16 RCAs, and 16 LCXs segments that had more than 40% stenosis were examined. For each frame, an expert manually segmented the plaque by tracing the vessel wall and lumen borders, Fig. 7(a). We performed our algorithm on 512×512 segmented frames that only contained plaque textures and selected Lemarie–Battle filters of order 17, expansion level $l = 2$ and the initial number of classes $N_c = 4$ (calcified, fibrotic, lipidic, and no tissue). The main advantage of ISODATA, over our previously developed framework based on k -means clustering algorithm [18], is that the clusters were merged if one or two tissues (out of three; lipidic, fibrotic, and calcified) were not presented within a plaque. We resolved the splitting case since we did not want to classify tissues beyond four typical atherosclerotic tissues classes. Finally, the resulting classified images were transformed into the Cartesian coordinates. Fig. 7 demonstrates a CSI, corresponding H&E histology image, and resulting PH image. The blue, yellow, and magenta colors exhibit calcified, fibrotic, and lipidic plaque components, respectively.

For quantification, histology is the best available version of ground truth for *in vitro* tissue characterization. However, the interpretation of histology images can often vary among experts yielding a subjective process. As a result, plaque constitutes can

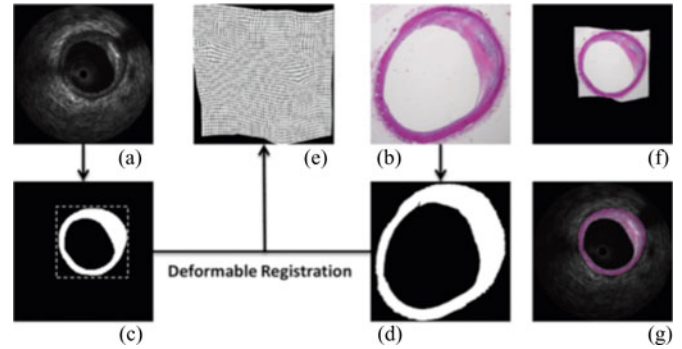


Fig. 8. Example of deformable registration process. Image (a) IVUS, (b) histology, (c) segmentation of IVUS, (d) segmentation of histology, (e) deformation field from histology to IVUS, (f) deformation applied to histology, and (g) visual overlap of deformed histology to IVUS.

be separated into fibrotic, lipidic, necrotic core, and calcified while another may differentiate between the levels of presence of fatty materials and add fibro-lipidic to compromise between fibrotic and lipidic. Due to the nature of the unsupervised classification approach, we evaluated the algorithm performance by asking an independent histopathologist to contrast the PH images with histology correspondences and score them. Previously, we deployed the same intuitive quantification method that relied on perceptual transformation of the most visually recognizable homogenous regions for each tissue types on a histology image onto IVUS grayscale image counterpart. For higher accuracy, we registered IVUS-histology images so the histopathologist could more confidently toggle between registered histology and PH images and use composite scoring in four quadrants [see Fig. 7(b) and (c)]. For example, in this particular case, 90% of fibrotic tissues were correctly classified while 3% and 7% of them were misclassified into calcified and lipidic tissues, respectively.

The registration could be challenging not only because of underlying differences between two imaging modalities, but also due to deformations introduced during histology preparation as well as acquisition process (*i.e.*, shrinkage). Nevertheless, a registration of intermediate image representations is feasible. Hence, we generated segmentation masks corresponding to lumen and media-adventitia borders for both histology and IVUS images and employed nonrigid registration with discrete Markov-random-field (MRF) objective function and approximate curvature penalty as smoothness regularization [27]. The resulting deformation field was applied to the original histology image to transfer it to the IVUS coordinate system. As we can see, the registered image [see Fig. 8(g)] is easier and more reliable to be used for scoring, labeling, and extracting features corresponding to each tissue type. The more comprehensive description of registration process is provided in [28]. Table II demonstrates the average values for correct and misclassified tissues in 83 CSIs with $60.57 \pm 12.49\%$ stenosis. For example, the first row shows that 99.60% (206884 pixels) of calcified labels in PH images correctly represented classified tissues in histology images while 0.32% (665 pixels) and 0.08% (166 pixels) of them were misclassified on average as fibrotic and

TABLE II
PERCENTAGE OF CORRECT CLASSIFICATION AS WELL AS MISCLASSIFICATION FOR EACH TISSUE TYPE ALONG WITH THEIR MINIMUM AND MAXIMUM RATES

	Ca n=207,715	F n=559,739	L n=801,350	No Tissue
Ca	99.60±1.62	0.32±1.46	0.08±0.42	0.00±0.00
max	100	10	3	0
min	90	0	0	0
F	7.17±5.61	87.70±6.28	5.16±2.78	0.15±0.03
max	25	100	12	3
min	0	70	0	0
L	1.89±2.83	6.50±2.76	90.78±4.13	0.74±1.17
max	15	15	100	5
min	0	0	80	0

(Ca: calcified; F: fibrotic; L: lipidic). *n* is total number of samples.

TABLE III
CLASSIFICATION RESULTS DRIVEN FROM MANUAL LABELS (TREATED AS GROUND TRUTH) AND CORRESPONDING REGIONS IN PH IMAGES

	ACC	SP	SE
Ca (33 CSIs) n=42,664	88.52±9.02	93.93±5.51	34.23±17.65
F (44 CSIs) n=230,494	73.93±12.36	63.90±12.40	43.21±12.85
L (40 CSIs) n=84,551	82.17±15.99	77.42±21.19	53.59±19.63
N (23 CSIs) n=60,084	59.36±16.31	55.61±18.25	62.75±24.92

Classification accuracy (ACC), specificity (SP), and sensitivity (SE). Necrotic (N).

lipidic, respectively. The overall classification performance has been evaluated to be 99.60%, 87.75%, and 90.87% for calcified, fibrotic, and lipidic tissues, respectively.

To further investigate the reliability of manual traced labels, drawn by the same histopathologist, and study the heterogeneity of atherosclerotic tissues, we evaluated the classified tissues in PH images and computed classification accuracy, specificity, and sensitivity. For this reason, for each tissue type, the labeled region [see Fig. 5(c)] was used as ground truth to quantify the same classified tissue in corresponding region in the PH image and the true positive (TP) along with false negative (FN) rates were computed. Subsequently, the false positive (FP), and true negative (TN) rates were measured, deploying the remaining labels as ground truth. Table III shows the statistics driven from 33, 44, and 23 CSIs for calcified, fibrotic, lipidic, and necrotic tissues, respectively. As we can see, the overall classification accuracy (ACC) has been decreased in comparison with those reported in Table II and the specificity (SP) as well as sensitivity (SE) are relatively low that could be associated with tissues heterogeneities, confirming the challenge of manual labeling. The most reliable manually traced labels were found to be for calcified tissues (high accuracy and specificity with low variations) that were expected since calcified regions repeatedly presented very well in IVUS images with high intensities.

In general, our texture-derived algorithm provides encouraging results; however, we do not intend to claim that the tissue characterization problem is solved. In order to achieve this, further investigation is required. There are important factors that need to be validated to extend any *in vitro* derived classifier, regardless of its type (supervised or unsupervised), for *in vivo* classification. For example, effects of blood and change of pressure on constructed tissue colormaps, consistency among tissue

colormaps in successive frames that practically substantiate the reliability of extracted tissues features [29], [30]. The main contribution of this study is replacing manual labeling with a systematic framework and offering a methodology that provides tissue colormaps with high correlation with histology images independent of IVUS transducer center frequency. In the following section, we will study the reliability of classification of tissues behind arc of calcified plaques where presence of adequate signal energy is dubious and apply our algorithm on *in vivo* collected data deploying 20 MHz Eagle Eye VOLCANO transducer to further validate our proposed algorithm against the state-of-the-art VH technique [7].

A. Classification of Tissues Behind Arc of Calcified Plaques

To validate classification of tissues in shadowed areas and in particular behind arc of calcified plaques through our confidence estimation framework described in Section III-B, we asked an expert to manually select low confidence (LC) and high confidence (HC) regions in histology images where severe ultrasound attenuation is expected (e.g., regions with dense calcified plaques) or not (e.g., fibrotic, fibro-lipidic tissues), respectively. As illustrated in Fig. 9(b), there is an apparent intraframe distinction between HC and LC regions whereas the interframe difference is not very explicitly distinctive. This is expected due to the fact that ultrasound travels through different mediums and paths to reach the HC and LC regions. The larger variance in some CSIs could be due to severe deformations between images that demand for more robust registration algorithm. We repeated the experiment on additional 16 CSIs collected from ten cadaver hearts with $59 \pm 36^\circ$ arc of calcified tissues in plaques with 60% burden and computed confidence values were found to be $93 \pm 80\%$, $76 \pm 14\%$, $57 \pm 13\%$, and $16 \pm 6\%$ in saline, well insonified plaques, normal plaques, and shadowing regions, respectively. Because of presence of guide-wire and therefore the shadowing behind it, the average value was a bit lower than expected in saline. The immediate conclusion is low reliability of regions behind arc of calcified plaques validated via our confidence estimation approach and confirmed by histology images. Fig. 10 demonstrates an IVUS grayscale image, corresponding confidence map, registered histology, and PH image before and after weighting with confidence values. Note that the confidence map does not entirely reject the availability of signals in LC regions and it is only a measure of reliability or so called confidence. This is also inferred in Fig. 9(b) where the LC values are “low” and not “zero” but when we go further away from dense calcified surface, the confidence values are more decreased and no textural information is perceived as shown in the PH image (3–5 o’clock for calcified plaque and 12 o’clock due to presence of guide wire) [see Fig. 10(d)]. In general, the systematic classification of tissues in regions behind arc of calcified plaques is not valid and could be misleading in clinical practice. However, we shall not exclude these regions without interpretation since they may carry out leading information toward VPs. The best is to come up with a visualization tool and enlighten interventional cardiologist to pay special attention to these regions when looking at and interpreting tissue colormaps.

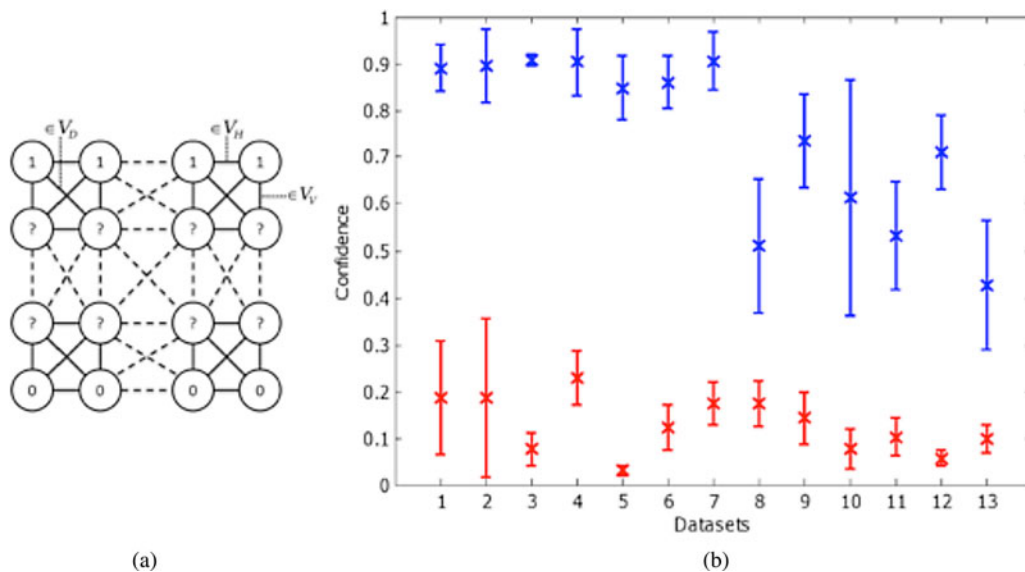


Fig. 9. (a) Eight-connected Laplacian graph with automatic seed placement. Virtual transducer element nodes are marked with unity and “no signal” nodes with zero potential. Confidence values calculated from manually selected HC (blue) and LC (red) regions in 13 cross sections by expert.

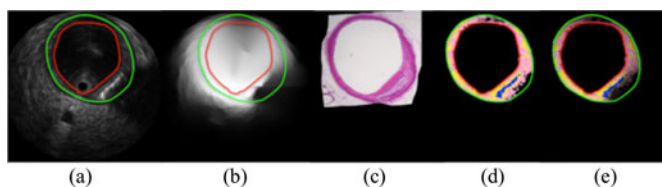


Fig. 10. (a) IVUS grayscale image with arc of calcified plaque at 3–5 o’clock and (b) corresponding confidence map, (c) registered histology, (d) PH image before and (e) after weighting with confidence values.

B. Comparison With the VH Algorithm

To better assess our proposed technique, we performed it on 174 grayscale images acquired *in vivo* from four patients, deploying 20-MHz transducer. We did not access to RF data but corresponding VH images were available and used for comparison and quantification in terms of correlation among tissues. Fig. 11 shows the resulting PH and VH images from three distinct IVUS frames. Given four tissues classes, we were able to generate tissue colormaps very close to VH images and found $93.1 \pm 6.1\%$, $87.5 \pm 9.5\%$, $78.4 \pm 17.6\%$, and $61.3 \pm 21.1\%$ correlation among calcified, necrotic, fibrotic, and fibrofatty tissues.

The results were of interest particularly from two points of views. First, we found the highest correlation among calcified that was not very surprising because it is often the easiest tissue to detect, and necrotic components. The latter becomes important since it can be a sign toward identification of VP. One may realize an arising controversy where we were not able to label necrotic tissues in PH images, constructed from images/RF signals collected with 40-MHz transducer, whereas, we showed detected necrotic employing 20-MHz grayscale images. Second, easing the “no tissue” label will lead to systematic detection of fibrofatty tissues in acoustic shadowing regions behind arc of calcified plaques, which is also noticeable in VH results. To

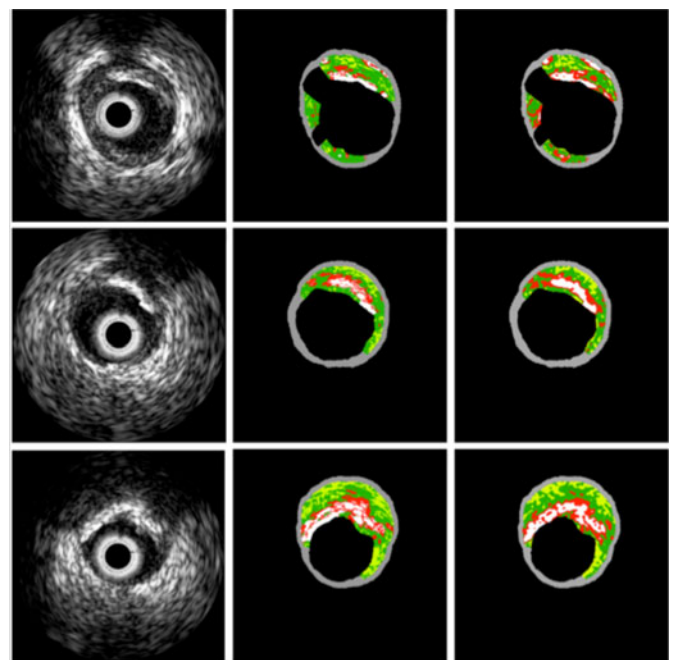


Fig. 11. Three distinct IVUS grayscale images (left column), corresponding VH (middle column), and PH (right column) images.

resolve this limitation, we weighted the classification results by use of measured confidence values as described in Section III-B.

Fig. 12 demonstrates the resulting weighted PH and VH images corresponding to Fig. 11 (bottom row). As we can see, there are visible textural patterns in the grayscale image [see Fig. 12(a)], behind calcified arc; however, the confidence map and weighted tissue colormaps imply that classification in this region is not reliable. Similar patterns are also found after liver–lung and tissue–bone interface where most of ultrasound energy is expected to reflect back [38] and experts entirely exclude these regions from their interpretations.

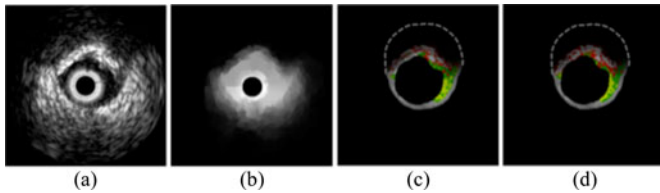


Fig. 12. IVUS grayscale image with arc of calcified plaque from 9 to 2 o'clock [(a) Fig. 11 lower left image], corresponding confidence map (b), and resulting weighted VH (c) as well as PH (d) images with confidence values. The gray dashed border is the MA contour drawn from the original VH image (see Fig. 11, bottom row, middle).

Comparing with histology images, when applied our algorithm on *in vitro* data collected with 40-MHz transducer, we found no correlation among PH results and necrotic tissue and concluded that we were not able to detect it by use of textural features only. The main reason is that necrotic core does not appear with any particular speckles patterns and often are echolucent, depending on the stage of formation. In other words, there is a transition in the formation of necrotic core from stage that collagen starts to be diminished and replaced by lipid within preserved (lipid pool) or degraded (necrotic core) extracellular matrix [39]. Recalling VP definition, we can infer vulnerability from PH images, similar to [19], where lipid pool is formed beneath the plaque and close to vessel wall (MA border). However, the direct detection of necrotic core in PH images requires more advanced technique, extracting additional features and employing supervised classification. We also examined 892 histology images collected from 12 arteries in 12 cadaver hearts and found that only 156 (17.5%) of them contained necrotic whereas this rate was 155/155 (100%) for all *in vivo* frames [37]. Histology showed $1.6 \pm 2.6\%$ of necrotic tissues per artery, whereas it was $10.1 \pm 21.8\%$ in the VH images. Necrotic appears to be overestimated in the VH image while histology shows that it is a rare tissue. We observed that the necrotic pattern in VH was sparse (along lateral direction and around calcified plaques) whereas histology showed it was confluent (toward vessel wall). Often, the VH necrotic pattern is due to rapid attenuation of IVUS signals in calcified plaques and is not related to tissue characteristics as confirmed by PH-histology cross validation. The same argument is also valid when we look at PH images. Our findings are in concordance with those in [39] and we conclude that precise detection of necrotic core is still ambiguous in IVUS-based existing atherosclerotic tissue characterization algorithms.

V. CONCLUSION

In this paper, we have presented a method for atherosclerotic tissue labeling in IVUS images. The objective of this study was to provide knowledge beyond the visible log-compressed B-mode IVUS assisting in clinical diagnosis. The iterative self-organizing behavior of the label clustering algorithm for lesion-type identification helps us to achieve the objective of visualizing the multiscalar colocalized tissue heterogeneity as evidently observed in biological structures. Furthermore, we have illustrated the importance of inclusion of a measure of ultrasonic signal confidence estimated using random walks, which plays

significant role in minimizing ambiguities on account of erroneous labeling of structures appearing in regions with severely attenuated ultrasonic penetration. One of the main advantages of the proposed algorithm is that it can be performed on RF signals or grayscale images independent of transducer center frequency. Even with an improved performance of this method in comparison with other available techniques, there are few open questions still to be addressed for answering completeness in understanding of underlying ultrasonic dynamics in imaged tissues. Superior state-of-the-art machine learning techniques employed for understanding the intertwined relation of ultrasonic frequency independent characteristics of different tissue would be close to achieving this objective and would open up multiple windows of research opportunities.

ACKNOWLEDGMENT

The authors would like to thank reviewers for their constructive comments and feedbacks and the Boston Scientific Corporation (Fremont, CA) for providing us the 40-MHz acquisition system. They would also like to thank J. Lisauskas and Dr. S. Sum at InfraRedx (Burlington, MA) who developed the artery fixation cage and helped in collecting IVUS data. The histology samples were processed at CVPPath (Gaithersburg, MD) under supervision of Dr. R. Virmani.

REFERENCES

- [1] American Heart Association, Heart Disease and Stroke Statistics—2010 update, American Heart Association, Dallas, TX, 2010.
- [2] E. Falk, "Why do plaques rupture?," *Circulation*, vol. 86, pp. III30–III42, 1992.
- [3] R. Virmani, A. P. Burke, F. D. Kolodgie, and A. Farb, "Pathology of the thin-cap fibroatheroma: A type of vulnerable plaque," *J. Interven. Cardiol.*, vol. 16, no. 3, pp. 267–272, 2003.
- [4] C. L. Korte, A. F. W. van der Steen, E. I. Céspedes, G. Pasterkamp, S. G. Carlier, F. Mastik, A. H. Schoneveld, P. W. Serruys, and N. Bom, "Characterization of plaque components and vulnerability with intravascular ultrasound elastography," *Phys. Med. Biol.*, vol. 45, pp. 1465–1475, 2000.
- [5] R. L. Maurice, J. Fromagea, M. R. Cardinal, M. Doyley, E. de Muinck, J. Robb, and G. Cloutier, "Characterization of atherosclerotic plaques and mural thrombi with intravascular ultrasound elastography: A potential method evaluated in an aortic rabbit model and a human coronary artery," *IEEE Trans. Inf. Technol. Biomed.*, vol. 12, no. 3, pp. 290–298, May 2008.
- [6] M. Kawasaki, H. Takatsu, T. Noda, K. Sano, Y. Ito, K. Hayakawa, K. Tsuchiya, M. Arai, K. Nishigaki, G. Takemura, S. Minatoguchi, T. Fujiwara, and H. Fujiwara, "In vivo quantitative tissue characterization of human coronary arterial plaques by use of integrated backscatter intravascular ultrasound and comparison with angioscopic findings," *Circulation*, vol. 105, no. 21, pp. 2487–2492, May 2002.
- [7] A. Nair, B. D. Kuban, M. Tuzcu, P. Schoenhagen, S. E. Nissen, and D. G. Vince, "Coronary plaque classification with intravascular ultrasound radiofrequency data analysis," *Circulation*, vol. 106, no. 17, pp. 2200–2206, 2002.
- [8] F. L. Lizzi, M. Greenebaum, E. J. Feleppa, M. Elbaum, and D. J. Coleman, "Theoretical framework for spectrum analysis in ultrasonic tissue characterization," *J. Acoust. Soc. Amer.*, vol. 73, pp. 1366–1373, 1983.
- [9] A. Katouzian, S. Sathyanarayana, B. Baseri, E. E. Konofagou, and S. G. Carlier, "Challenges in atherosclerotic plaque characterization with intravascular ultrasound (IVUS): From data collection to classification," *IEEE Trans. Inf. Technol. Biomed.*, vol. 12, no. 3, pp. 315–327, May 2008.
- [10] J. M. Tobis, J. Mallery, D. Mahon, K. Lehmann, P. Zalesky, J. Griffith, J. Gessert, M. Moriuchi, M. McRae, and M. L. Dwyer, "Intravascular ultrasound imaging of human coronary arteries *in vivo*. Analysis of tissue characterization with comparison to *in vitro* histological specimens," *Circulation*, vol. 83, pp. 913–926, 1991.

- [11] K. Gad and M. B. Leon, "Characterization of atherosclerotic lesions by intravascular ultrasound: Possible role in unstable coronary syndromes and in interventional therapeutics procedure," *Amer. J. Cardiol.*, vol. 68, pp. 85B–91B, 1991.
- [12] X. Zhang, C. R. McKay, and M. Sonka, "Tissue characterization in intravascular ultrasound images," *IEEE Trans. Med. Imag.*, vol. 17, no. 6, pp. 889–899, Dec. 1998.
- [13] K. L. Caballero, O. Pujol, J. Barajas, J. Mauri, and P. Radeva, "Assessing in-vivo IVUS tissue classification accuracy between normalized image reconstruction and RF analysis," in *Proc. MICCAI*, 2006, pp. 82–89.
- [14] S. Escalera, O. Pujol, J. Mauri, and P. Radeva, "Intravascular ultrasound tissue characterization with sub-class error-correcting output codes," *J. Sign. Process. Syst.*, vol. 55, pp. 35–47, 2009.
- [15] A. Taki, H. Hetterich, A. Roodaki, S. K. Setarehdan, G. Unal, J. Rieber, N. Navab, and C. A. Konig, "A new approach for improving coronary plaque component analysis based on intravascular ultrasound images," *Ultrasound Med. Biol.*, vol. 36, no. 8, pp. 1245–1258, 2010.
- [16] J. Seabra, F. Ciompi, O. Pujol, J. Mauri, P. Radeva, and J. Sanchez, "Rayleigh mixture model for plaque characterization in intravascular ultrasound," *IEEE Trans. Biomed. Eng.*, vol. 58, no. 5, pp. 1314–1324, May 2011.
- [17] A. Katouzian and A. F. Laine, "Methods in atherosclerotic plaque characterization using intravascular ultrasound (IVUS) images and backscattered signals," in *Atherosclerosis Disease Management*. Berlin, Germany: Springer, pp. 121–152, 2010.
- [18] A. Katouzian, B. Baseri, E. Konofagou, and A. F. Laine, "Texture-driven coronary artery plaque characterization using wavelet packet signatures," in *Proc. 5th IEEE Int. Symp. Biomed. Imag.: Nano Macro*, 2008, pp. 197–200.
- [19] M. Okubo, M. Kawasaki, Y. Ishihara *et al.*, "Tissue characterization of coronary plaques: comparison of integrated backscatter intravascular ultrasound with virtual histology intravascular ultrasound," *Circulation*, vol. 72, pp. 1631–1639, 2008.
- [20] K. Tanaka, S. G. Carlier, A. Katouzian, and G. Mintz, "Characterization of the intravascular ultrasound radio frequency signal within regions of acoustic shadowing behind calcium," *J. Amer. Coll. Cardiol.*, vol. 49, no. 9, Suppl. B, p. 29B, 2007.
- [21] G. S. Mintz and E. Missel, "What is behind the calcium? The relationship between calcium and necrotic core on virtual histology analyses: Reply," *Eur. Heart J.*, vol. 30, pp. 125–126, 2009.
- [22] A. F. Laine and J. Fan, "Frame representation for texture segmentation," *IEEE Trans. Image Proc.*, vol. 5, no. 5, pp. 771–780, May 1996.
- [23] A. Katouzian, S. Sathyanarayana, W. Li, T. Thomas, and S. G. Carlier, "Challenges in tissue characterization from backscattered intravascular ultrasound signals," in *IEEE Proc. SPIE*, San Diego, vol. 65130, Feb. 2007, pp. 65130-1–65130-8.
- [24] R. R. Coifman and M. V. Wickerhauser, "Entropy-based algorithms for best basis selection," *IEEE Trans. Inform. Theory*, pt. II, vol. 38, no. 2, pp. 713–718, Mar. 1992.
- [25] S. G. Mallat, "A theory of multiresolution signal decomposition: The wavelet representation," *IEEE Trans. Patt. Anal. Mach. Intell.*, vol. 11, no. 7, pp. 674–693, Jul. 1989.
- [26] R. O. Duda, P. E. Hart, and D. G. Stork, *Unsupervised learning and clustering*, Ch. 10 in *pattern classification*, 2nd ed. New York: Wiley, 2001.
- [27] B. Glocker, N. Komodakis, G. Tziritas, N. Navab, and N. Paragios, "Dense image registration through MRFs and efficient linear programming," *Med. Image Anal.*, vol. 12, no. 6, pp. 731–741, 2008.
- [28] A. Katouzian, A. Karamalis, J. Lissauskas, A. Eslami, and N. Navab, "IVUS-histology image registration," presented at the 5th workshop on biomedical image registration, Nashville, TN, pp. 141–149.
- [29] A. Katouzian, A. Karamalis, A. Laine, and N. Navab, "A systematic approach toward reliable atherosclerotic plaque characterization in IVUS images," in *Bildverarbeitung für die Medizin*. Berlin, Germany: Springer, 2012.
- [30] A. Katouzian and S. Carlier, "Development and performance of a new unsupervised classifier for IVUS-based tissue characterization," in *Proc. 31st Annu. Scientific Meeting Belgian Soc. Cardiol.*, 2012.
- [31] K. Tanaka, S. G. Carlier, A. Katouzian, and G. Mintz, "Characterization of the intravascular ultrasound radiofrequency signal within regions of acoustic shadowing behind calcium," *J. Amer. Coll. Cardiol.*, vol. 49, no. 9, Suppl. B, p. 29B, 2007.
- [32] G. S. Mintz and E. Missel, "What is behind the calcium? The relationship between calcium and necrotic core on virtual histology analyses: Reply," *Eur. Heart J.*, vol. 30, pp. 125–126, 2009.
- [33] A. Taki, A. Roodaki, O. Pauly, S. Setarehdan, G. Unal, and N. Navab, "A new method for characterization of coronary plaque composition via ivus images," in *Proc. IEEE Int. Symp. Biomed. Imaging: From Nano to Macro (ISBI)*, Jun./Jul. 2009, pp. 787–790.
- [34] A. Karamalis, W. Wein, T. Klein, and Nassir Navab, "Ultrasound confidence maps using random walks," *J. Med. Imag. Analysis*, doi: <http://dx.doi.org/10.1016/j.media.2012.07.005>
- [35] A. Karamalis, S. Carlier, A. Katouzian, and N. Navab, "Confidence estimation in IVUS radio-frequency data with random walks," in *IEEE Int. Symp. Biomed. Imaging (ISBI): From Nano to Macro*, May 2012, pp. 1068–1071.
- [36] Richard S. C. Cobbold, *Foundations of Biomedical Ultrasound*. London, U.K.: Oxford University Press, 2006.
- [37] A. Katouzian, A. Karamalis, A. Koenig, S. Carlier, and N. Navab, "Ambiguity in detection of necrotic in IVUS plaque characterization algorithms," *Eur. Soc. Cardiol.*, 2012.
- [38] Hedrick, Hykes, and Starchman, "Ultrasound Physics and Instrumentation," 4th ed., Amsterdam, The Netherlands: Elsevier MOSBY.
- [39] T. Thim, M. K. Hagensen, D. W. Bradley, J. F. Granada, G. L. Kaluza, L. Drouet, W. P. Paaske, H. E. Bøtker, and E. Falk, "Unreliable assessment of necrotic core by virtual histology intravascular ultrasound in porcine coronary artery disease," *Circulation Card. Imag.*, vol. 3, pp. 384–391, 2010.
- [40] F. Ciompi, O. Pujol, C. Gatta, O. Rodríguez-Leor, J. Mauri-Ferre, and P. Radeva, "Fusing in-vitro and in-vivo intravascular ultrasound data for plaque characterization," *Int. J. Cardiovasc. Imaging*, vol. 26, no. 7, pp. 763–779, 2010.

Authors' photographs and biographies not available at the time of publication.